



HAL
open science

Light-driven Electrodynamics and Demagnetization in Fe_nGeTe₂ (n = 3, 5) Thin Films

Luca Tomarchio, Vincent Polewczyk, Lorenzo Mosesso, Alain Marty, Salvatore Macis, Matthieu Jamet, Frédéric Bonell, Stefano Lupi

► **To cite this version:**

Luca Tomarchio, Vincent Polewczyk, Lorenzo Mosesso, Alain Marty, Salvatore Macis, et al.. Light-driven Electrodynamics and Demagnetization in Fe_nGeTe₂ (n = 3, 5) Thin Films. npj 2D Materials and Applications, 2024, 8 (1), pp.73. hal-04616460v2

HAL Id: hal-04616460

<https://hal.science/hal-04616460v2>

Submitted on 9 Dec 2024

HAL is a multi-disciplinary open access archive for the deposit and dissemination of scientific research documents, whether they are published or not. The documents may come from teaching and research institutions in France or abroad, or from public or private research centers.

L'archive ouverte pluridisciplinaire **HAL**, est destinée au dépôt et à la diffusion de documents scientifiques de niveau recherche, publiés ou non, émanant des établissements d'enseignement et de recherche français ou étrangers, des laboratoires publics ou privés.



Distributed under a Creative Commons Attribution - NonCommercial - NoDerivatives 4.0 International License

<https://doi.org/10.1038/s41699-024-00510-8>

Light-driven electrodynamics and demagnetization in Fe_nGeTe_2 ($n = 3, 5$) thin films

Check for updates

Luca Tomarchio¹, Vincent Polewczyk², Lorenzo Mosesso¹, Alain Marty², Salvatore Macis¹,
Matthieu Jamet², Frédéric Bonell² & Stefano Lupi¹ ✉

Two-dimensional materials-based ultrafast spintronics are expected to surpass conventional data storage and manipulation technologies, that are now reaching their fundamental limits. The newly discovered van der Waals (VdW) magnets provide a new platform for ultrafast spintronics since their magnetic and electrical properties can be tuned by many external factors, such as strain, voltage, magnetic field, or light absorption for instance. Here, we report on the direct relationship between magnetic order and Terahertz (THz) electrodynamics in Fe_nGeTe_2 ($n = 3, 5$) (FGT) films after being illuminated by a femtosecond optical pulse, studying their ultrafast THz response as a function of the optical pump-THz probe temporal delay. In Fe_5GeTe_2 , we find clear evidence that light-induced electronic excitations directly influence THz electrodynamics similarly to a demagnetization process, contrasting with the effects observed in Fe_3GeTe_2 , which are characterized by a thermal energy transfer among electrons, magnons, and phonons. We address these effects as a function of the pump fluence and pump-probe delay, and by tuning the temperature across the magnetic ordering Curie temperature, highlighting the microscopic mechanisms describing the out-of-equilibrium evolution of the THz conductivity. Finally, we find evidence for the incoherent-coherent crossover predicted by the Kondo-Ising scenario in Fe_3GeTe_2 and successfully simulate its light-driven electrodynamics through a three-temperature model. As indicated by these results, FGT surpasses conventional metals in terms of modulating their properties using an optical lever.

The extensive study of Fe_nGeTe_2 ($n = 3, 5$) (FGT) materials is driven by their two-dimensional van der Waals (VdW) nature and the high-temperature ferromagnetic properties. Van der Waals magnets may sustain novel phases of matter, like the Quantum anomalous Hall Effect^{1–3} or the spin liquid state⁴. Moreover, their magnetic properties can be tuned through different degrees of freedom like thickness^{5,6}, atomic composition^{7,8}, or gating bias^{9,10}. In contrast to the firstly discovered 2D magnets like CrI_3 ^{11–13} and $\text{Cr}_2\text{Ge}_2\text{Te}_6$ ¹⁴, FGT compounds possess higher critical temperatures, up to room temperature^{15,16}. For this reason, FGT is suitable for integration into van der Waals magnetic heterostructures, paving the way for high-temperature spintronic research and applications based on these devices^{17–22}.

FGT has a layered centrosymmetric crystal structure that depends on the number $n = 3, 5$ of Fe atoms in the unit cell^{15,16}, in which Fe and Ge sublattices are sandwiched between two Te layers along the c axis. This

number is critical in determining the magnetic and electrodynamical properties of the FGT compounds. For instance, when $n = 3$, Fe_3GeTe_2 (F3GT) belongs to the $P63/mmc$ space group, and the Fe I atoms arrange in a hexagonal lattice containing only Fe atoms (see Fig. 1a). Fe II and Ge atoms are instead covalently bonded in an adjacent layer^{23,24}. Fe_5GeTe_2 (F5GT) crystallizes in the rhombohedral $R\bar{3}m$ space group, with a larger unit-cell due to the inclusion of excess Fe atoms¹⁵. The additional Fe atoms strengthen the magnetization due to the creation of a 3D exchange network similar to a 3D Heisenberg model²⁵, enhancing the exchange interaction and resulting in a larger Curie temperature ($T_c \sim 300$ K)^{15,26,27} with respect to F3GT ($T_c \sim 230$ K). The 3D nature of intralayer magnetic interactions hinders the perpendicular magnetic anisotropy (PMA), which is absent in bulk F5GT^{15,27,28}, whereas F3GT exhibits a single hard magnetic phase with a near square-shaped magnetic loop, large coercivity^{29,30}, and a large PMA increasing monotonously with decreasing temperatures^{9,19}. As revealed by

¹Department of Physics, Sapienza University, Rome, Italy. ²University Grenoble Alpes, CNRS, CEA, IRIG-Spintec, Grenoble, France.

✉ e-mail: stefano.lupi@roma1.infn.it

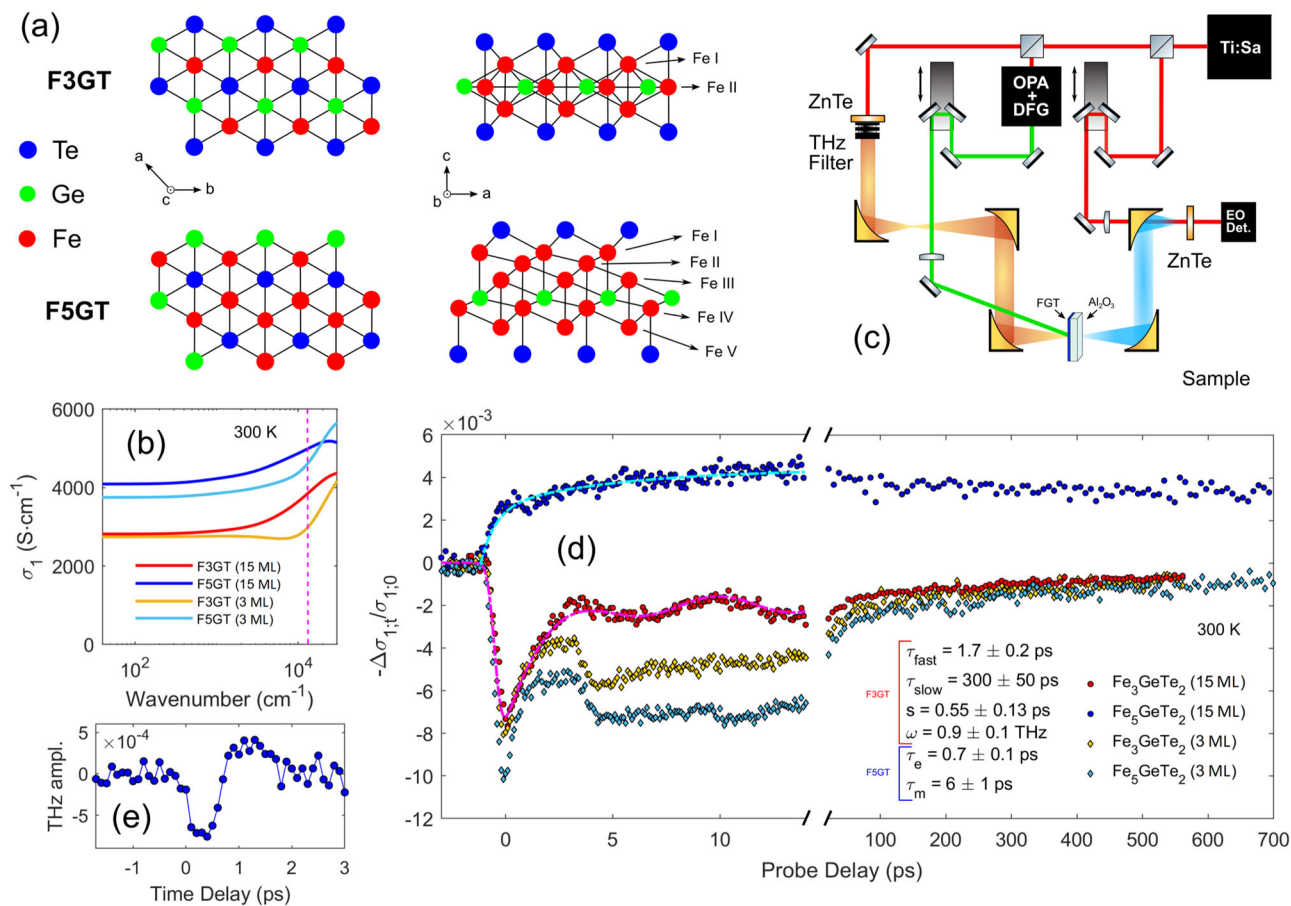


Fig. 1 | Crystal structure and optical pump-THz probe measurements of Fe_nGeTe₂ (n = 3, 5) films. **a** Crystal structure as seen from two different points of view for Fe₃GeTe₂ (F3GT) and Fe₅GeTe₂ (F5GT). For simplicity, the Fe I atoms are represented only near the Te top plane. In reality, they are distributed near both Te layers, forming two partially occupied sub-lattices^{15,27}. **b** Real part of optical conductivity for the four measured films, as extracted through a multi-layer stacking model. The pink dotted line identifies the 800 nm (12,500 cm⁻¹) pump wavelength. **c** Optical pump-THz probe spectroscopy setup. An initial seed laser (800 nm, 30 fs, 7 mJ) is split twice to create a probe THz signal through optical rectification in a ZnTe

crystal (0.5 mm), a pump signal at variable wavelength through an optical parametric amplifier and difference frequency generation (OPA+DFG) system, and a final optical signal to probe the THz electric field through an electro-optical (EO) detection in a second ZnTe crystal (0.3 mm). **d** Pump-probe data at 300 K and 5 mJ/cm² for the four measured films over an extended time scale. The discontinuous curves overlaid to the experimental data represent the best fits according to Eq. (1) and a bi-exponential type-II demagnetization, respectively for the 15 ML F3GT and F5GT films. The best-fit parameters are indicated in the inset. **e** Light-induced demagnetization THz emission from a 15 ML F5GT film.

other studies, both materials appear to host additional magnetic phases like anti-ferromagnetism^{31,32} (F3GT) and ferrimagnetism²⁸ (F5GT), and complex magnetic structures like skyrmions^{33,34} for F3GT, and butterfly-shaped MR³⁵ and high-density meron textures³⁶ for F5GT.

From an electro-dynamical perspective, both systems are strongly correlated ferromagnetic metals, where quantum fluctuation effects are crucial for a correct description of the ground state³⁷. For instance, Kondo physics at low temperatures has been clearly found in F3GT and recently similar effects have been observed in F5GT³⁸. Deviations from the itinerant Stoner model are more prominent in F3GT^{39,40}, where local magnetic moments play a crucial role at low temperatures, establishing a Kondo-Ising scenario^{41,42}, mediated by an incoherent-coherent crossover ($T \sim 100$ K) where the *3d* conduction electrons hybridize with the local moments^{43,44}. The mass increase of the conduction electrons leads to electro-dynamical changes such as a strong increase in the Sommerfeld coefficient^{8,37} and a transfer of optical spectral weight toward lower frequencies⁴⁵. Besides the Kondo physics, FGT also exhibits strong electron-phonon (e-ph) coupling^{15,46} and large anomalous Hall effect, which are linked to the presence of topological nodal states^{45,47,48} and an enhanced skew scattering⁴⁹, respectively for F3GT and F5GT.

Given the plethora of magnetic and electro-dynamical features of FGT compounds, their growth and characterization as thin films are yearned for technological applications. We already showed in refs. 22,27 that growth by

molecular beam epitaxy yields high-quality F3GT and F5GT films with robust magnetism in the ultrathin limit. In this work, instead, we make use of optical pump-THz probe spectroscopy (OPTPS) to study the out-of-equilibrium dynamics of conductive electrons in F3GT and F5GT thin films, addressing the light-induced changes that appear in the material's phase after being illuminated by a femtosecond optical pulse, on a time scale ranging from sub-ps to hundreds of picoseconds. We observe stark differences in the THz photoconductivity between the magnetic and non-magnetic phases, suggesting a strong dependence of the electronic transport on the magnetic ordering. Given the magnetic properties and differences between F3GT and F5GT, we discuss the light-induced THz response in terms of electro-dynamical and demagnetization effects. Moreover, the time variation of the photoconductivity and its dependence on the pump properties, like fluence and polarization, shine a light on the mechanisms that describe the magnetization evolution in FGT, as induced by Stoner excitations, Elliot-Yafet spin flips, or magnon formation, and their correlation to the THz conductivity through electron-spin interactions.

Experimental results and discussion

Optical properties

FGT films were prepared by molecular beam epitaxy (MBE) in an ultra-high vacuum deposition system²⁷. Four films were prepared onto 500 μm thick Al₂O₃ (0001) substrates (see methods): two F3GT films of thickness 15

monolayers (ML) and 3 ML (1 ML ~ 0.81 nm), and two F5GT films of thickness 15 ML and 3 ML (1 ML ~ 0.97 nm). Magnetic characterization of the films with magneto-optical Kerr effect is provided in the Supplementary Information (SI). The samples' optical properties were initially measured through the study of their optical reflectance (R) across a broad spectral range, from THz (40 cm^{-1}) to visible ($25,000\text{ cm}^{-1}$) (see methods). The R data are shown in Supplementary Fig. 1a. To analyze the behavior of the FGT films, it is necessary to consider the optical response of the substrate. To do so, the Al_2O_3 substrate data were analyzed through a Kramers-Kronig (KK) constrained fitting to extract its complex optical refraction index⁵⁰ (the resulting optical indices for Al_2O_3 are shown in Supplementary Fig. 1b). The optical data are then modeled in terms of an air/film/substrate trilayer⁵¹ and fitted through the RefFit program⁵⁰ (more information can be found in the section "Multi-layer Stacking Model" of the SI). The real part of the optical conductivity is shown in Fig. 1b (the imaginary part in Supplementary Fig. 1d). The conductivity data suggests a metallic behavior for the FGT films, as already observed in F3GT single crystals⁴⁵. The flat behavior at low frequencies can be described by a broad Drude term, whose plasma frequency is higher for the F5GT compound. In contrast to bulk F3GT, where the Drude plasma frequency is $\omega_p \sim 800\text{ cm}^{-1}$ ⁴⁵, in thin films the Drude contribution extends toward higher frequencies, smoothly mixing with the activation of interband transitions (see Supplementary Table 1 in the SI). The DC conductivity extracted from the optical data is comparable to the resistivity measurements obtained using a van der Pauw 4-probes geometry (see Supplementary Table 2).

Room temperature optical pump-THz probe spectroscopy

The control of films' conductivity through light on very short time scales (below 1 ns) can cast light over the electronic transient physical processes at irradiation, namely, charge transport and the subsequent interaction of electrons with lattice and spin degrees of freedom. After a short optical pulse, electrons are excited from a valence band state to a conduction band state, and their evolution in time can be sampled with a second probe pulse in the THz range.

To study the temporal dynamics of the FGT charge carriers in a sub-ps time scale, an ultrashort optical pulse (30 fs) with wavelength centered at 800 nm has been used. Upon changing the pumping wavelength, from 400 nm to 10 μm , no modification to the out-of-equilibrium evolution of the FGT films was observed. Therefore, only the 800 nm data are reported in this work to avoid redundancy. Fig. 1c represents the optical setup used for the pump-probe experiment. Here, two delay lines are used to tune respectively the time delay between the pump and THz signal on the sample, and the THz and probe signal on an electro-optical detector (see methods). After the pump arrives, the photoinduced current is probed by a THz pulse in a transmission configuration. More specifically, the transmitted THz electric field change $\Delta E_t = E_t - E_0$ is measured as a function of the pump-probe delay time t between the optical and THz signal, where E_t and E_0 denote the peak value of the THz electric field at a delay time t and without the pump, respectively. In the thin film approximation, the photoinduced relative transmission change $\Delta E_t/E_0$ is proportional to the THz negative photoconductivity (PC) $-\Delta\sigma_{1,t}/\sigma_{1,0}$, where σ_1 is the real part of the optical conductivity. No external magnetic field has been applied to the samples during the optical measurements.

Figure 1d shows $\Delta E_t/E_0 = -\Delta\sigma_{1,t}/\sigma_{1,0}$ for the four FGT films at 300 K when pumped with a $5\text{ mJ}/\text{cm}^{-2}$ linearly polarized pulse at 800 nm. The time axis is separated into two parts to highlight the temporal behavior in a short and long time window. Different behaviors for the photoinduced response can be identified depending on the sample compound and thickness. The thinner (3 ML) F3GT and F5GT films show an almost equal trend in time, with only a change in magnitude probably due to the difference in their THz conductivity (see Fig. 1b). For the thicker films (15 ML), instead, the evolution in time shows an opposite trend: the conductivity of the F3GT film increases (decrease in THz transmission) similarly to the 3 ML films while the conductivity of the F5GT film decreases, with a very slow decay to equilibrium after an initial upward trend reaching its peak at ~ 20 ps.

During the pump illumination, the energy is transferred from the photons to the charge carriers (the electrons) of the system. This rapid process, where an out-of-equilibrium regime is created, is sequentially followed by a fast thermalization of the electron bath to a higher temperature through electron-electron scattering. This process may take up to 1 ps, depending on the material⁵², and is readily observed in Fig. 1d for the 3 ML films of F3GT and F5GT, and for the 15 ML film of F3GT, as a negative change of the THz transmission trace (positive change in conductivity). After this first fast process, the electron bath dissipates its energy toward the lattice, forcing a decay to equilibrium that can be as slow as a few nanoseconds, depending on the material thermal conductivity, thickness, and substrate interaction⁵³. Moreover, during the energy transfer toward the lattice, acoustic phonons are created through the electron-phonon coupling (thermoelastic effect)⁵⁴. The presence of a strain pulse of coherent acoustic phonons traveling inside the material is observed as oscillations in the pump-probe dynamics, which can take the shape of sinusoidal waves like the one observed in Fig. 1d for the 15 ML F3GT (~ 1 THz) after 3 ps. Similar but less intense oscillations are observed in the 3 ML films, after a fast change in the pump-probe trace at nearly 3 ps. This latter effect is not fully understood. Previous results revealed the emergence of light-driven room-temperature ferromagnetism in thin F3GT⁵⁵, induced by the enhancement of the T_c through the Stoner criterion after a redistribution of the electronic states. As will be discussed later, the induced magnetization could contribute to the THz conductivity giving rise to the feature at 3 ps (see Fig. 1d). The rise and decay processes of the out-of-equilibrium dynamics described above can be modeled with a sum of exponential terms convoluted with an activation term that describes the rising edge of the photoinduced transient. The fitting model takes the form⁵⁶

$$\Delta E_t/E_0 = \sum_i a_i \exp(-t/\tau_i) \left(1 - \text{erf} \left(\frac{-4t\tau_i + s^2}{2\sqrt{2s}\tau_i} \right) \right) \quad (1)$$

where a_i are the amplitudes of the different decay components, τ_i are the respective relaxation times, erf is the error function, and s is the effective rise time. Assuming two decay components (τ_{fast} and τ_{slow}) and an additional oscillatory term $\cos(\omega t + \varphi)$, the best-fitting curve for the experimental data in Fig. 1d of the 15 ML F3GT film is shown as a pink discontinuous curve overlaid to the data. The fitting parameters are reported as an inset in the same Figure. An extended Figure, up to 30 ps, is shown in Supplementary Fig. 4b. Two scattering times ($\tau_{fast} = 1.7 \pm 0.2\text{ ps}$, $\tau_{slow} = 300 \pm 50\text{ ps}$) are ascribed to the electron and lattice temperature decays, respectively, and the rising edge $s = 0.55 \pm 0.13\text{ ps}$ to the electronic temperature increase. The extracted oscillation frequency is $\omega = 0.9 \pm 0.1\text{ THz}$.

Until now the analysis has focused on F3GT (3 and 15 ML) and F5GT (3 ML), which share the paramagnetic phase at 300 K (see Supplementary Fig. 3 for the magnetization curves). In contrast, the 15 ML F5GT film possesses a higher Curie temperature ($T_c \sim 300\text{ K}$) and is instead in a ferromagnetic phase. This difference in magnetic order is readily appreciated by the opposite trend in the pump-probe trace as shown in Fig. 1d. The sample conductivity does not increase after illumination, but rather decreases following a two-step process: a fast change lasting less than 1 ps, and a slow evolution to its maximum value at ~ 20 ps. This trend cannot be described by Eq. (1), but rather by a sequence of two exponential functions, usually used to describe the two-step laser-induced demagnetization processes indicative of type-II demagnetization, similar to rare-earth ferromagnets Gd and Tb^{57,58}, as well as the VdW magnet $\text{Cr}_2\text{Ge}_2\text{Te}_6$ ⁵⁹. By defining τ_e and τ_m as the characteristic timescales for the fast and slow processes, the best fit gives $\tau_e = 0.7 \pm 0.1\text{ ps}$, which is a typical value for the electron-phonon relaxation in ferromagnetic transition metals⁶⁰, and $\tau_m = 6 \pm 1\text{ ps}$, ascribed to the demagnetization timescale. The fitting curve is shown as a discontinuous light-blue curve overlaid to the data in Fig. 1d. The interaction of femtosecond laser pulses with magnetic thin films induces a wide range of out-of-equilibrium phenomena, leading to an ultrafast demagnetization, and subsequent magnetization dynamics. However, these effects are usually observed through magneto-optical Kerr effect (MOKE)

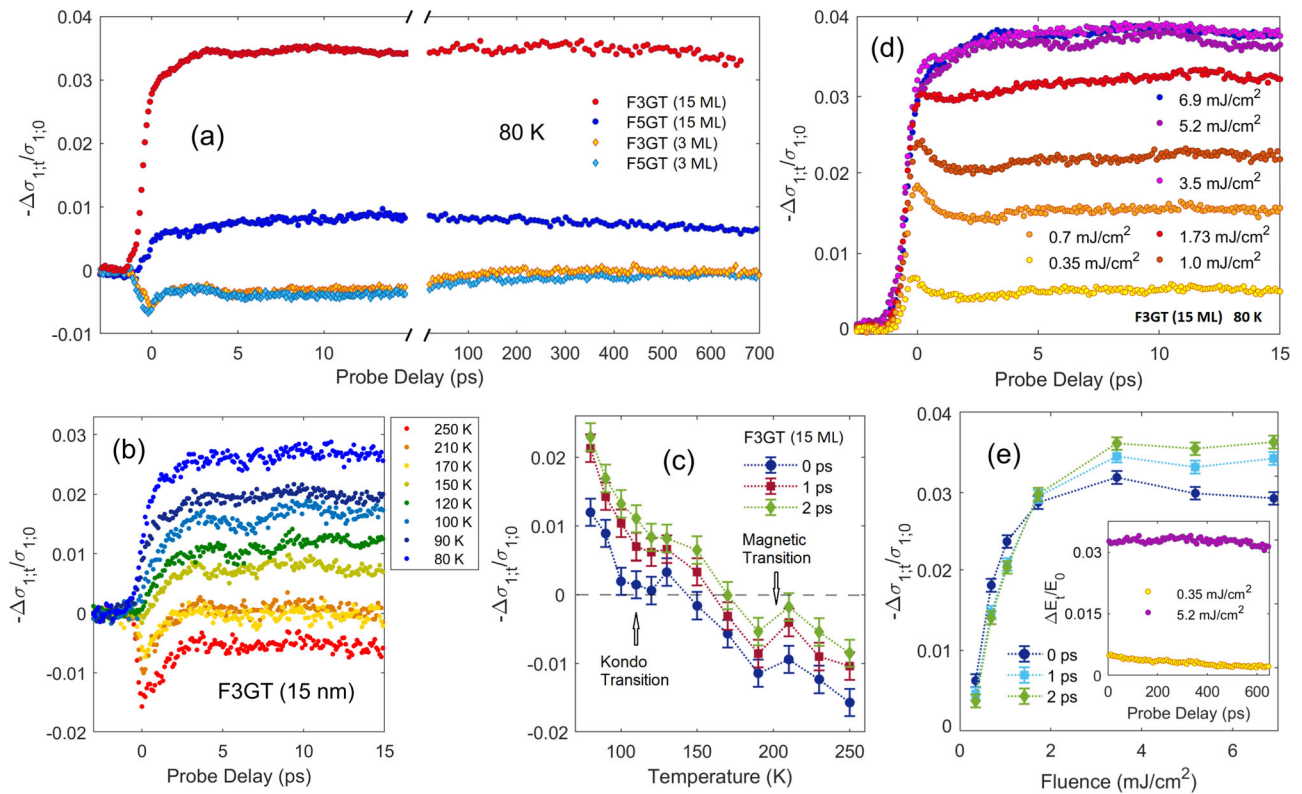


Fig. 2 | Optical pump-THz probe measurements of Fe_nGeTe_2 ($n = 3, 5$) films at different temperatures and fluences. **a Pump-probe data at 80 K and 5 mJ/cm^2 for the four measured films over an extended time scale. **b** Pump-probe trace at different temperatures (heating from 80 K) for the 15 ML F3GT film. **c** Temperature evolution of the pump-probe trace at fixed probe delays 0, 1, and 2 ps of **b**. The arrows indicate the magnetic and Kondo lattice transition of F3GT. **d** Pump-probe data at 80 K and**

variable fluence for the 15 ML F3GT film. **e** Fluence evolution of the 80 K pump-probe trace of F3GT (15 ML) at fixed probe delays 0, 1, and 2 ps of **d**. The inset shows the extension at longer probe delays of **d** for two fluences. Data error bars shown in panels **c** and **d** were obtained from the average and the standard deviation of 30 measured pump-probe traces, each one consisting of 100 acquisitions for each point.

spectroscopy, whose results have been proven to be proportional to the magnetization even outside equilibrium⁶¹. The fact that it is possible to observe the magnetization dynamics with such clarity through THz spectroscopy suggests a direct relationship between the magnetization state and the electrons' conductivity in F5GT. This effect is even more striking when considering the absence of an external magnetic field during the experiment, meaning that it relies only on the spontaneous magnetization of the sample. The ultrafast demagnetization hypothesis can also be supported by the observation of THz generation. Demagnetization effects are usually accompanied by a THz emission process at the pump arrival due to the oscillation of magnetic dipoles⁶². Such an effect, shown in Fig. 1e in terms of the THz amplitude vs time delay, is observed at the pump arrival for F5GT when the probe THz beam is blocked.

Light-induced demagnetization effects in magnetic films are driven by two types of effects: a reduction of the magnetic moment carried by each atom, and a random tilt of the magnetic moment of each atom, resulting in a cancellation of the average magnetization⁶³. However, to date, there is no consensus regarding the main source of demagnetization, and these processes are material-dependent⁶³. The reduction of the magnetic moment is due to the creation of Stoner excitations, resulting from a decrease of the exchange splitting⁶⁴, or Elliot-Yafet spin-flips⁶⁵, while the tilt is a consequence of the creation of magnons by a direct energy transfer through the electron-spin or lattice-spin coupling. The observation of rapid (sub-picosecond) demagnetization behavior in the THz photoconductivity of F5GT suggests that the carriers play a central role in driving demagnetization, aligning with the concept of Stoner excitations. This also implies that the magnetic order itself directly influences the low-energy electrodynamic, probably through a sensitive change in the electron scattering. This process is qualitatively different from what is found in standard ferromagnetic

films^{63,66,67}, where the demagnetization is mainly driven by the production of magnons through a thermal transfer from the excited mobile electrons (positive photoconductivity after pump). A possible direct interaction of the photon field with the spins (an "all-optical switching"⁶⁸) is rejected on the basis of its helicity dependence. Indeed, no changes in the pump-probe trace are observed when pumping the system with a circularly polarized light.

Low temperature measurements

To further prove the ultrafast demagnetization hypothesis, the pump-probe measurements were repeated at 80 K, below the F3GT Curie temperature (~230 K). The results are shown in Fig. 2a. The key difference with respect to the 300 K data is the F3GT (15 ML) response, which changes sign and shows a process similar to F5GT (15 ML) but with a magnitude nearly 5 times higher. This change appears near the Curie temperature, as can be seen in the temperature-dependent traces shown in Fig. 2b and the fixed probe delay values in Fig. 2c, suggesting a direct contribution of the magnetic order on the THz conductivity also for F3GT. The thinner films, instead, although ferromagnetic at 80 K (see Supplementary Fig. 3), keep showing the same behavior as in the paramagnetic phase. This difference can be attributed to the weaker spontaneous magnetization associated with the thinner (3 ML) films²⁷. As anticipated in the previous section, the light-induced enhancement of the T_c through the Stoner criterion can produce a net spontaneous magnetization in these films⁵⁵, affecting the low-energy electrodynamic as already proved in the 15 ML samples, and addressing the 3 ps features observed at both 300 K and 80 K.

The pump-probe trace of F3GT (15 ML) is quantitatively and qualitatively different from the F5GT (15 ML). The latter shows only a magnitude change after decreasing the temperature, as expected for a demagnetization process in standard ferromagnets⁶⁹. The F3GT trace, instead, shows a rapid

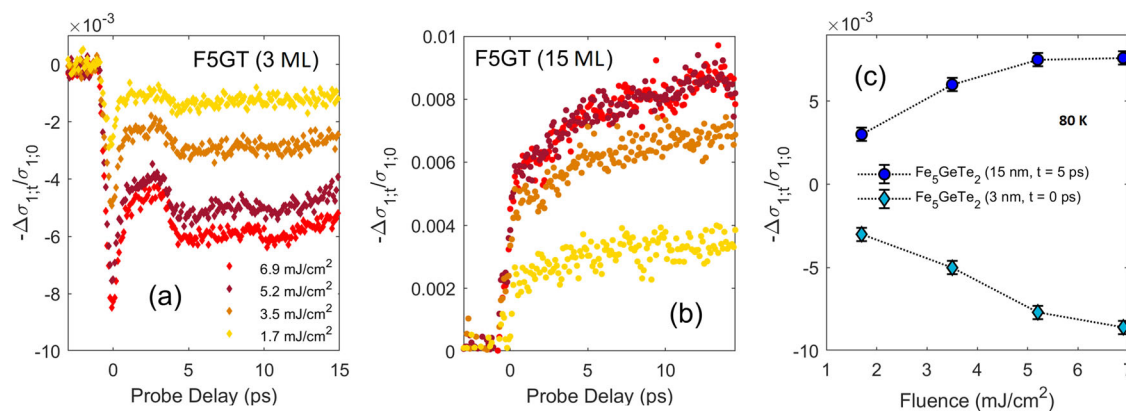


Fig. 3 | Optical pump-THz probe fluence-dependent measurements of Fe_5GeTe_2 films. a, b Fluence dependence of the 80 K pump-probe trace for F5GT films of 3 and 15 ML, respectively. **c** Fluence evolution of the pump-probe trace at fixed probe delays for the 3 and 15 ML films of F5GT at 80 K.

increase followed by a slower (nearly 3 ps) increase to a flat equilibrium modified by slow fluctuations like the ones observed for the 300 K trace, which have been associated with the propagation of acoustic phonon modes. The magnetic properties of F3GT are different from those of F5GT, with F3GT having a strong magnetic anisotropy along the *c*-axis. This suggests that spontaneous magnetization can be higher in F3GT, accounting for the increase in the magnitude of the THz conductivity change. In F3GT, magnon formation can be a driver for demagnetization. Recent pump-probe MOKE experiments of F3GT flakes⁷⁰ have shown how the demagnetization effect can be associated with an angular momentum transfer between the electron, phonon, and spin subsystems. However, the pump-probe MOKE traces differ from the THz conductivity here reported. Indeed, for the F3GT electrodynamics, additional complexity is given by the presence of a second phase transition taking place in F3GT at 100 K, which is an incoherent-coherent crossover leading to a Kondo scenario⁴² that can be observed also in the pump-probe trace (see Fig. 2c) as a modulation near 100 K. In this phase, the itinerant electrons couple to the localized magnetic moments increasing their effective mass and leading to electro-dynamical changes^{8,45}.

Further insights on the F3GT THz photoconductivity contributions are obtained by measuring the pump-probe trace as a function of the pump fluence. Fig. 2d and e show the results for the 15 ML F3GT. As a function of fluence, the pump-probe spectrum in Fig. 2d shows a rapid transition from a peaked trace to a smooth rising one, suggesting the co-existence of both light-induced hot carriers and demagnetization effects, accounting for the trace peak and the slow rise, respectively. The data highlights a transition from a hot-carriers-dominated effect to a demagnetization-dominated effect, going from low to high fluences. This transition is highlighted in Fig. 2e, showing how the 0 ps trace (peak position in Fig. 2d) decreases at higher fluences.

A possible explanation for the F3GT trace behavior comes from the Kondo ordering and thermal energy transfer, as described by a 3-temperature model (3TM). At 80 K, F3GT conduction electrons are affected by the Kondo effect, increasing their effective mass and mobility due to the elastic scattering by a lattice of local magnetic moments⁷¹. After illumination, the electrons are driven out of this coherent state due to their rising temperature, decreasing their conductivity. This effect is readily seen in Fig. 2c, where the THz transmission increases rapidly below 100 K. Other possible explanations for the negative photoconductivity observed might come from the dynamical formation of quasiparticles like polarons. However, for FGT, no such formation can be highlighted. Analogously, Stoner excitations are excluded since the observed effect has a clear temperature activation that is far away from the Curie temperature, while instead matching the Kondo-Ising scenario (~100 K).

The hot electrons that form after illumination alone also induce a demagnetization in the magnetized layer⁶³. At high fluences, this

demagnetization can be attributed to a transfer of heat from the hot electrons to the lattice, causing the system to cross the Curie temperature and exit the ferromagnetic phase. At low fluences, instead, demagnetization effects are still present as suggested by MOKE experiments⁷⁰, and can be linked to the increase in the magnon bath's temperature, which reduces the F3GT average magnetization. Longitudinal demagnetization effects like Stoner excitations are still possible, but it has been shown that in metallic systems their effect is secondary with respect to magnons⁶³ and a dominant magnon+Elliot-Yafet demagnetization picture has been proved for F3GT⁷⁰. Given the magnon demagnetization picture, already proved for F3GT, 3TM simulations, comprising the electron, magnon, and lattice thermal baths, were performed to understand the changes in the pump-probe trace as a function of fluence, as described in the SI. The resulting temperatures are shown in Supplementary Fig. 5a–c, highlighting the thermal transfer from electrons to magnons at low fluences, and the heating above T_c of the lattice at high fluences. The higher the fluence, the faster the system exits the magnetic state. This effect explains the disappearance of the peak from the THz trace above 1.7 mJ/cm² (see Fig. 2d), being substituted by the phase change dynamics at early times. The phase change effect is also in accordance with the experimental data at longer times, since the relaxation to equilibrium becomes very slow, of the order of nanoseconds, as shown in Fig. 2a and the inset of Fig. 2e for a 5 mJ/cm² fluence.

Finally, Fig. 3a and b show the results for the 3 and 15 ML F5GT, while the time fixed-changes are shown in Fig. 3c. The F5GT samples show only quantitative changes as a function of fluence, where the response of the 15 ML film saturates already at 5 mJ/cm², while the one of the 3 ML film seems to increase linearly. The latter observation is in accordance with the increased production of free carriers after pumping, while the former shows an increase of τ_m with fluence, similar to other FGT crystals⁷⁰, where the electron-phonon scattering event leads to a spin-flip (Elliot-Yafet mechanism) due to the presence of spin-orbit coupling. Indeed, at high enough fluences, the slow dynamics for the 15 ML F5GT crystal observed both at 80 K and 300 K can also be associated with the lattice heating after illumination, whose temperature reaches the Curie temperature. This induces a phase transition to the paramagnetic state, increasing the lifetime of the out-of-equilibrium state up to the ns scale.

Discussion

The presented experiments demonstrated that illumination of FGT films with ultrashort optical pumps causes significant changes in the THz photoconductivity related to the demagnetization effects and production of hot carriers. Depending on the thickness and chemical composition ($n = 3, 5$) of Fe_nGeTe_2 thin films, the pump-probe behavior changes as a result of the variance in the magnetic properties and electro-dynamical ordering between the different films. In particular, light-induced demagnetization effects in Fe_5GeTe_2 are found in THz transmission measurements, which are linked

to a change of the longitudinal magnetization on a sub-ps time-scale through a decrease of the exchange splitting, and followed by a slower demagnetization trend induced by Elliot-Yafet spin-flips and the ferromagnetic-to-paramagnetic phase transition at high pump fluences. Substantial differences are obtained for the pump-probe trace of Fe_3GeTe_2 , as caused by the production of hot carriers and their thermal exchange to magnons and the underlying lattice. Finally, temperature-dependent measurements demonstrated the sensitivity of optical pump-THz probe measurements to the magnetic and Kondo lattice ordering in Fe_3GeTe_2 . The present results concern the interaction of light with the small spontaneous magnetization in FGT films. Future experiments under an applied magnetic field could bring further insights into the mechanisms of light-induced THz conductivity changes. The dependence of the electrodynamic properties on the magnetization state observed in this work indicates FGT compounds as candidate materials for the study of proximity effects in heterostructures and the production of tunable electro-optical and spintronic devices.

Methods

Sample preparation

The FGT films were grown by MBE on $\text{Al}_2\text{O}_3(0001)$ substrates by co-evaporation of high-purity Fe, Ge, and Te, as reported in ref. 27. The composition of the films (F3GT or F5GT) was adjusted by setting the Fe:Ge flux ratio to the desired stoichiometry, while keeping an over-stoichiometric Te flux. The substrate temperature during growth was 300 °C for F3GT and 350 °C for F5GT. After the deposition, the films were annealed at 550 °C under Te flux in order to improve their crystallinity, then capped at room temperature with a 3-nm-thick Al film that was naturally oxidized in air. $\theta/2\theta$ X-ray diffraction scans shown in SI confirm that both F3GT and F5GT films are single-phase, with the expected c lattice parameter.

Optical characterization

Reflectance measurements at room temperature (RT) were taken through a Vertex 70v FTIR broadband interferometer, covering the spectral range from THz (40 cm^{-1}) to mid-infrared (MIR) (7000 cm^{-1}), and through a Jasco V-770 spectrometer, extending the spectral data from 5000 cm^{-1} up to the visible (VIS) region ($20,000\text{ cm}^{-1}$). Optical pump-terahertz probe measurements were developed in a transmission geometry through the generation of THz pulses from a ZnTe (110) crystal (0.5 mm thick), whose electric field is detected in a time-domain experimental configuration through an electro-optical sampling in a second ZnTe (0.3 mm thick). All measurements were performed in vacuum. The signal covers a range of frequencies going from 0.6 THz to ~2.5 THz. It is generated by a 800 nm pulse (7 mJ) with a time duration of 35 fs, as obtained by a Ti:sapphire amplifier (Coherent® Verdi G-series), with a repetition rate of 1 kHz. The signals used to pump the films along with the THz are obtained from the 800 nm itself which can be used directly or sent to an optical parametric amplifier (OPA) (TOPASprime from Light Conversion®) for the generation of wavelengths from 1200 nm and 2400 nm wavelengths. A consecutive difference frequency generator (DFG from Light Conversion®) takes in input the OPA output and generates wavelengths ranging from 2600 to 16,000 nm. A lens is used to focus the pump pulse onto the sample position. A 400 nm pump has also been obtained from the second harmonic generation of the 800 nm signal into a BBO nonlinear crystal. The THz detection is achieved through an electro-optical scheme based on the Pockels effect induced by the THz radiation itself in a ZnTe crystal. The change in birefringence is probed through an 800 nm pulse overlapping in time and space with the THz pulse in the detection crystal. The polarization change is then measured via a balanced photodiode.

Data availability

The datasets used and/or analyzed during the current study are available from the corresponding author on reasonable request.

Received: 14 February 2024; Accepted: 27 October 2024;

Published online: 12 November 2024

References

1. Tokura, Y., Yasuda, K. & Tsukazaki, A. Magnetic topological insulators. *Nat. Rev. Phys.* **1**, 126–143 (2019).
2. Chang, C.-Z. et al. Experimental observation of the quantum anomalous hall effect in a magnetic topological insulator. *Science* **340**, 167–170 (2013).
3. Tomarchio, L. et al. Electrodynamic of MnBi_2Te_4 intrinsic magnetic topological insulators. *NPG Asia Mater.* **14**, 82 (2022).
4. Knolle, J., Kovrizhin, D., Chalker, J. & Moessner, R. Dynamics of a two-dimensional quantum spin liquid: signatures of emergent Majorana fermions and fluxes. *Phys. Rev. Lett.* **112**, 207203 (2014).
5. Gong, C. et al. Discovery of intrinsic ferromagnetism in two-dimensional van der Waals crystals. *Nature* **546**, 265–269 (2017).
6. Huang, B. et al. Layer-dependent ferromagnetism in a van der Waals crystal down to the monolayer limit. *Nature* **546**, 270–273 (2017).
7. Verchenko, V. Y., Tsirlin, A. A., Sobolev, A. V., Presniakov, I. A. & Shevelkov, A. V. Ferromagnetic order, strong magnetocrystalline anisotropy, and magnetocaloric effect in the layered Telluride Fe_3GeTe_2 . *Inorg. Chem.* **54**, 8598–8607 (2015).
8. May, A. F., Calder, S., Cantoni, C., Cao, H. & McGuire, M. A. Magnetic structure and phase stability of the van der Waals bonded ferromagnet $\text{Fe}_{3-x}\text{GeTe}_2$. *Phys. Rev. B* **93**, 014411 (2016).
9. Deng, Y. et al. Gate-tunable room-temperature ferromagnetism in two-dimensional Fe_3GeTe_2 . *Nature* **563**, 94–99 (2018).
10. Jiang, S., Li, L., Wang, Z., Mak, K. F. & Shan, J. Controlling magnetism in 2D CrI_3 by electrostatic doping. *Nat. Nanotechnol.* **13**, 549–553 (2018).
11. Tomarchio, L. et al. Low energy electrodynamic of CrI_3 layered ferromagnet. *Sci. Rep.* **11**, 23405 (2021).
12. Tomarchio, L. et al. Phonon anharmonicity and spin-Phonon coupling in CrI_3 . *Materials* **16**, 4909 (2023).
13. Huang, B. et al. Electrical control of 2D magnetism in bilayer CrI_3 . *Nat. Nanotechnol.* **13**, 544–548 (2018).
14. Yang, D. et al. $\text{Cr}_2\text{Ge}_2\text{Te}_6$: High thermoelectric performance from layered structure with high symmetry. *Chem. Mater.* **28**, 1611–1615 (2016).
15. May, A. F. et al. Ferromagnetism near room temperature in the cleavable van der Waals Crystal Fe_5GeTe_2 . *ACS Nano* **13**, 4436–4442 (2019).
16. Fei, Z. et al. Two-dimensional itinerant ferromagnetism in atomically thin Fe_3GeTe_2 . *Nat. Mater.* **17**, 778–782 (2018).
17. Wang, X. et al. Current-driven magnetization switching in a van der Waals ferromagnet Fe_3GeTe_2 . *Sci. Adv.* **5**, eaaw8904 (2019).
18. Chen, X. et al. Generation and control of terahertz spin currents in topology-induced 2D ferromagnetic $\text{Fe}_3\text{GeTe}_2|\text{Bi}_2\text{Te}_3$ Heterostructures. *Adv. Mater.* **34**, 2106172 (2022).
19. Li, Q. et al. Patterning-Induced ferromagnetism of Fe_3GeTe_2 van der Waals materials beyond room temperature. *Nano Lett.* **18**, 5974–5980 (2018).
20. Liu, S. et al. Wafer-scale two-dimensional ferromagnetic Fe_3GeTe_2 thin films grown by molecular beam epitaxy. *npj 2D Mater. Appl.* **1**, 30 (2017).
21. Tan, C. et al. Gate-controlled magnetic phase transition in a van der Waals magnet Fe_5GeTe_2 . *Nano Lett.* **21**, 5599–5605 (2021).
22. Guillet, T. et al. Spin-Orbit torques and magnetization switching in $(\text{Bi,Sb})_2\text{Te}_3/\text{Fe}_3\text{GeTe}_2$ heterostructures grown by molecular beam epitaxy. *Nano Lett.* [acs.nanolett.3c03291](https://pubs.acs.org/doi/10.1021/acs.nanolett.3c03291) <https://pubs.acs.org/doi/10.1021/acs.nanolett.3c03291> (2024).
23. Deiseroth, H., Aleksandrov, K., Reiner, C., Kienle, L. & Kremer, R. K. Fe_3GeTe_2 and Ni_3GeTe_2 - Two new layered transition-metal compounds: crystal structures, HRTEM investigations, and magnetic and electrical properties. *Eur. J. Inorg. Chem.* **2006**, 1561–1567 (2006).
24. Chen, B. et al. Magnetic properties of layered itinerant electron ferromagnet Fe_3GeTe_2 . *J. Phys. Soc. Jpn.* **82**, 124711 (2013).

25. Li, Z. et al. Magnetic critical behavior of the van der Waals $F_{65}GeTe_2$ crystal with near room temperature ferromagnetism. *Sci. Rep.* **10**, 15345 (2020).
26. Seo, J. et al. Nearly room temperature ferromagnetism in a magnetic metal-rich van der Waals metal. *Sci. Adv.* **6**, eaay8912 (2020).
27. Ribeiro, M. et al. Large-scale epitaxy of two-dimensional van der Waals room-temperature ferromagnet Fe_5GeTe_2 . *npj 2D Mater. Appl.* **6**, 10 (2022).
28. Ohta, T. et al. Enhancement of coercive field in atomically-thin quenched Fe_5GeTe_2 . *Appl. Phys. Express* **13**, 043005 (2020).
29. Tan, C. et al. Hard magnetic properties in nanoflake van der Waals Fe_3GeTe_2 . *Nat. Commun.* **9**, 1554 (2018).
30. León-Brito, N., Bauer, E. D., Ronning, F., Thompson, J. D. & Movshovich, R. Magnetic microstructure and magnetic properties of uniaxial itinerant ferromagnet Fe_3GeTe_2 . *J. Appl. Phys.* **120**, 083903 (2016).
31. Kim, D. et al. Antiferromagnetic coupling of van der Waals ferromagnetic Fe_3GeTe_2 . *Nanotechnology* **30**, 245701 (2019).
32. Yi, J. et al. Competing antiferromagnetism in a quasi-2D itinerant ferromagnet: Fe_3GeTe_2 . *2D Mater.* **4**, 011005 (2016).
33. Birch, M. T. et al. History-dependent domain and skyrmion formation in 2D van der Waals magnet Fe_3GeTe_2 . *Nat. Commun.* **13**, 3035 (2022).
34. Ding, B. et al. Observation of magnetic Skyrmion bubbles in a van der Waals Ferromagnet Fe_3GeTe_2 . *Nano Lett.* **20**, 868–873 (2020).
35. Ohta, T. et al. Butterfly-shaped magnetoresistance in van der Waals ferromagnet Fe_5GeTe_2 . *AIP Adv.* **11**, 025014 (2021).
36. Lv, X. et al. Controllable topological magnetic transformations in the thickness-tunable van der Waals ferromagnet Fe_5GeTe_2 . *ACS Nano* **16**, 19319–19327 (2022).
37. Zhu, J.-X. et al. Electronic correlation and magnetism in the ferromagnetic metal Fe_3GeTe_2 . *Phys. Rev. B* **93**, 144404 (2016).
38. Huang, Y., Yao, X., Qi, F., Shen, W. & Cao, G. Anomalous resistivity upturn in the van der Waals ferromagnet Fe_5GeTe_2 . *Appl. Phys. Lett.* **121**, 162403 (2022).
39. Xu, X. et al. Signature for non-Stoner ferromagnetism in the van der Waals ferromagnet Fe_3GeTe_2 . *Phys. Rev. B* **101**, 201104 (2020).
40. Joe, M., Yang, U. & Lee, C. First-principles study of ferromagnetic metal Fe_5GeTe_2 . *Nano Mater. Sci.* **1**, 299–303 (2019).
41. Zhao, M. et al. Kondo holes in the two-dimensional itinerant ising ferromagnet Fe_3GeTe_2 . *Nano Lett.* **21**, 6117–6123 (2021).
42. Zhang, Y. et al. Emergence of Kondo lattice behavior in a van der Waals itinerant ferromagnet, Fe_3GeTe_2 . *Sci. Adv.* **4**, eaao6791 (2018).
43. Onuki, Y., Furukawa, Y. & Komatsubara, T. Dense Kondo behavior in $Ce_xLa_{1-x}Al_2$. *J. Phys. Soc. Jpn.* **53**, 2734–2740 (1984).
44. Gottwick, U. et al. Seebeck coefficient of heavy fermion compounds. *J. Magn. Magn. Mater.* **63–64**, 341–343 (1987).
45. Corasaniti, M. et al. Electronic correlations in the van der Waals ferromagnet Fe_3GeTe_2 revealed by its charge dynamics. *Phys. Rev. B* **102**, 161109 (2020).
46. Du, L. et al. Lattice Dynamics, phonon chirality, and spin-phonon coupling in 2D itinerant ferromagnet Fe_3GeTe_2 . *Adv. Funct. Mater.* **29**, 1904734 (2019).
47. Xu, J., Phelan, W. A. & Chien, C.-L. Large anomalous Nernst effect in a van der Waals ferromagnet Fe_3GeTe_2 . *Nano Lett.* **19**, 8250–8254 (2019).
48. Kim, K. et al. Large anomalous Hall current induced by topological nodal lines in a ferromagnetic van der Waals semimetal. *Nat. Mater.* **17**, 794–799 (2018).
49. Suzuki, R., Gao, T., Nakayama, H. & Ando, K. Extrinsic anomalous Hall effect in van der Waals ferromagnet Fe_5GeTe_2 . *AIP Adv.* **13**, 055311 (2023).
50. Kuzmenko, A. B. Kramers-Kronig constrained variational analysis of optical spectra. *Rev. Sci. Instrum.* **76**, 083108 (2005).
51. Heavens, O. S. Optical properties of thin films. *Rep. Prog. Phys.* **23**, 1–65 (1960).
52. Del Fatti, N. et al. Nonequilibrium electron dynamics in noble metals. *Phys. Rev. B* **61**, 16956–16966 (2000).
53. Giannetti, C. et al. Ultrafast optical spectroscopy of strongly correlated materials and high-temperature superconductors: a non-equilibrium approach. *Adv. Phys.* **65**, 58–238 (2016).
54. He, C. et al. Study of confined coherent acoustic phonon modes in a free-standing cubic GaN membrane by femtosecond spectroscopy. *Appl. Phys. Lett.* **107**, 112105 (2015).
55. Liu, B. et al. Light-tunable ferromagnetism in atomically thin Fe_3GeTe_2 driven by Femtosecond laser pulse. *Phys. Rev. Lett.* **125**, 267205 (2020).
56. Demsar, J., Sarrao, J. L. & Taylor, A. J. Dynamics of photoexcited quasiparticles in heavy electron compounds. *J. Phys.: Condens. Matter* **18**, R281–R314 (2006).
57. Vaterlaus, A., Beutler, T. & Meier, F. Spin-lattice relaxation time of ferromagnetic gadolinium determined with time-resolved spin-polarized photoemission. *Phys. Rev. Lett.* **67**, 3314–3317 (1991).
58. Si, M. S. & Zhang, G. P. Resolving photon-shortage mystery in femtosecond magnetism. *J. Phys.: Condens. Matter* **22**, 076005 (2010).
59. Zhang, T. et al. Laser-induced magnetization dynamics in a van der Waals ferromagnetic $Cr_2Ge_2Te_6$ nanoflake. *Appl. Phys. Lett.* **116**, 223103 (2020).
60. Koopmans, B. et al. Explaining the paradoxical diversity of ultrafast laser-induced demagnetization. *Nat. Mater.* **9**, 259–265 (2010).
61. Carva, K., Baláž, P. & Radu, I. Laser-Induced Ultrafast Magnetic Phenomena. In *Handbook of Magnetic Materials*, vol. 26, 291–463 (Elsevier, 2017). <https://linkinghub.elsevier.com/retrieve/pii/S1567271917300045>.
62. Beaurepaire, E. et al. Coherent terahertz emission from ferromagnetic films excited by femtosecond laser pulses. *Appl. Phys. Lett.* **84**, 3465–3467 (2004).
63. Scheid, P., Remy, Q., Lebègue, S., Malinowski, G. & Mangin, S. Light induced ultrafast magnetization dynamics in metallic compounds. *J. Magn. Magn. Mater.* **560**, 169596 (2022).
64. Scheid, P., Malinowski, G., Mangin, S. & Lebègue, S. Ab initio study of electronic temperature effects on magnetic materials properties. *Phys. Rev. B* **99**, 174415 (2019).
65. Essert, S. & Schneider, H. C. Electron-phonon scattering dynamics in ferromagnetic metals and their influence on ultrafast demagnetization processes. *Phys. Rev. B* **84**, 224405 (2011).
66. Beaurepaire, E., Merle, J.-C., Daunois, A. & Bigot, J.-Y. Ultrafast spin dynamics in ferromagnetic nickel. *Phys. Rev. Lett.* **76**, 4250–4253 (1996).
67. Schmidt, A. B. et al. Ultrafast Magnon generation in an Fe film on Cu(100). *Phys. Rev. Lett.* **105**, 197401 (2010).
68. Stanciu, C. D. et al. All-optical magnetic recording with circularly polarized light. *Phys. Rev. Lett.* **99**, 047601 (2007).
69. Roth, T. et al. Temperature dependence of laser-induced demagnetization in Ni: A key for identifying the underlying mechanism. *Phys. Rev. X* **2**, 021006 (2012).
70. Lichtenberg, T. et al. Anisotropic laser-pulse-induced magnetization dynamics in van der Waals magnet Fe_3GeTe_2 . *2D Mater.* **10**, 015008 (2023).
71. Coleman, P. Heavy Fermions and the Kondo Lattice: a 21st Century Perspective <http://arxiv.org/abs/1509.05769> (2015).

Acknowledgements

This research was supported by MUR PRIN project (PHOTO) 2020RPEPNH and by PNR MUR project grant number PE0000023-NQSTI. Spintec was supported by the FLAG-ERA grant MNEMOSYN, by ANR contracts ANR-21-GRF1-0005-01, ANR-20-CE24-0015, and by the LANEF framework (ANR-10-LABX-51-01) for mutualized infrastructure.

Author contributions

The project has been conceptualized and supervised by S.L. and F.B. Samples have been synthesized and characterized by V.P., A.M., F.B., and M.J. Reflectance measurements were carried out by L.T. and S.M. Optical pump–THz Probe measurements were carried out by L.T. and L.M. The data treatment and analysis were performed by L.T.; L.T. and S.L. prepared the original draft. All authors reviewed and edited the manuscript. All authors have read and agreed to the published version of the manuscript.

Competing interests

The authors declare no competing interests.

Additional information

Supplementary information The online version contains supplementary material available at

<https://doi.org/10.1038/s41699-024-00510-8>.

Correspondence and requests for materials should be addressed to Stefano Lupi.

Reprints and permissions information is available at <http://www.nature.com/reprints>

Publisher's note Springer Nature remains neutral with regard to jurisdictional claims in published maps and institutional affiliations.

Open Access This article is licensed under a Creative Commons Attribution-NonCommercial-NoDerivatives 4.0 International License, which permits any non-commercial use, sharing, distribution and reproduction in any medium or format, as long as you give appropriate credit to the original author(s) and the source, provide a link to the Creative Commons licence, and indicate if you modified the licensed material. You do not have permission under this licence to share adapted material derived from this article or parts of it. The images or other third party material in this article are included in the article's Creative Commons licence, unless indicated otherwise in a credit line to the material. If material is not included in the article's Creative Commons licence and your intended use is not permitted by statutory regulation or exceeds the permitted use, you will need to obtain permission directly from the copyright holder. To view a copy of this licence, visit <http://creativecommons.org/licenses/by-nc-nd/4.0/>.

© The Author(s) 2024